

Magnetized Disk-Winds in NGC 3783

KEIGO FUKUMURA^{1,2}, DEMOSTHENES KAZANAS³, CHRIS SHRADER^{3,4}, EHUD BEHAR⁵,

FRANCESCO TOMBESI^{3,6,7} AND IOANNIS CONTOPOULOS⁸

September 17, 2018

Received _____; accepted _____

¹Department of Physics and Astronomy, James Madison University, Harrisonburg, VA 22807; fukumukx@jmu.edu

²KITP Scholar at UC Santa Barbara

³Astrophysics Science Division, NASA/Goddard Space Flight Center, Greenbelt, MD 20771

⁴Catholic University of America, Washington, DC 20064

⁵Department of Physics, Technion, Haifa 32000, Israel

⁶Department of Astronomy and CRESST, University of Maryland, College Park, MD20742

⁷Department of Physics, University of Rome “Tor Vergata”, Via della Ricerca Scientifica 1, I-00133 Rome, Italy

⁸Research Center for Astronomy, Academy of Athens, Athens 11527, Greece

ABSTRACT

We analyze a 900-ks stacked *Chandra*/HETG spectrum of NGC 3783 in the context of magnetically-driven accretion-disk wind models in an effort to provide tight constraints on the global conditions of the underlying absorbers. Motivated by the earlier measurements of its absorption measure distribution (AMD) indicating X-ray-absorbing ionic columns that decrease slowly with decreasing ionization parameter, we employ 2D magnetohydrodynamic (MHD) disk-wind models to describe the global outflow. We compute its photoionization structure along with the wind kinematic properties allowing us to further calculate in a self-consistent fashion the shapes of the major X-ray absorption lines. With the wind radial density profile determined by the AMD, the profiles of the ensemble of the observed absorption features are determined by the two global parameters of the MHD wind; i.e. disk inclination θ_{obs} and wind density normalization n_o . Considering the most significant absorption features in the ($\sim 1.8 \text{ \AA} - 20 \text{ \AA}$) range, we show that the MHD-wind is best described by $n(r) \sim 6.9 \times 10^{11} (r/r_o)^{-1.15} \text{ cm}^{-3}$ and $\theta_{\text{obs}} = 44^\circ$. We argue that winds launched by X-ray heating, radiation pressure or even MHD winds but with steeper radial density profiles are strongly disfavored by data. Considering the properties of Fe K band absorption features (i.e. Fe XXV and Fe XXVI), while typically prominent in the AGN X-ray spectra, they appear to be weak in NGC 3783. For the specific parameters of our model obtained by fitting the AMD and the rest of absorption features, these features are found to be weak in agreement with observation.

Subject headings: accretion, accretion disks — galaxies: Seyfert — methods: numerical — galaxies: individual (NGC 3783) — (magnetohydrodynamics:) MHD

1. Introduction

Ionized outflows are a common feature of Active Galactic Nuclei (AGN), manifesting themselves as blue-shifted absorption spectral lines. Approximately 50% – 70% of all Seyfert 1’s exhibit such features in their UV spectra and a similar fraction in their X-ray spectra (Crenshaw, Kraemer & George 2003). The most likely process responsible for the outflowing plasma ionization is photoionization by the AGN ionizing continuum; in this respect, X-rays appear to be of broader utility in probing their properties since X-ray transitions span a much larger range in photoionization parameter ξ than the UV ones.

X-ray absorption features were discovered first in the *Einstein* QSO spectra (e.g. Halpern 1984), with more significant detections of K-shell absorption edges due to O VII (0.74 keV) and O VIII (0.87 keV) by *ROSAT* (Nandra & Pounds 1992; Nandra 1993; Fiore et al. 1993; Turner et al. 1993). Later on, the improved spectroscopic capabilities of *ASCA* confirmed the robust presence of these edges in many luminous Seyfert AGNs (e.g. Reynolds et al. 1997; George et al. 1998); attributed to absorption by warm plasmas ($T \sim 10^6$ K), they have been thenceforth referred to as Warm Absorbers (WA). With the much enhanced spectral resolution and sensitivity of dispersive spectrometers onboard *Chandra* and *XMM-Newton*, it became obvious that there exists a plethora of absorption lines of various charge states of many elements; these span a wide range of ionization parameter $\xi \equiv L_{\text{ion}}/(nr^2)$ (e.g. Crenshaw, Kraemer & George 2003; Blustin et al. 2005; Steenbrugge et al. 2005; McKernan et al. 2007) where L_{ion} is the ionizing (X-ray) luminosity, n is electron number density at radius r . Their columns lie in the range $10^{20} \lesssim N_H \lesssim 10^{22}$ cm $^{-2}$, their ionization parameter between $-1 \lesssim \log \xi \lesssim 4$, their temperatures between $10^4 < T < 10^7$ and the exhibit line-of-sight (LoS) velocities of $v/c \lesssim 0.01$ (e.g. Reynolds et al. 1995), implying distances $r \gtrsim 10^4$ Schwarzschild radii, employing the Keplerian association between velocity and radius.

NGC 3783 is a nearby ($z = 0.00976$), bright AGN with black hole mass of $3 \times 10^7 M_{\odot}$ (Peterson et al. 2004); it has been observed with *Chandra*/HETGS a number of times to date since 2000 (Kaspi et al. 2000), and also in conjunction with simultaneous observations by *ASCA* and *RXTE* (Kaspi et al. 2001, hereafter K01). It is one of the most intensively monitored Seyfert galaxies for its high-resolution absorption study with a total duration of 900 ks *Chandra* grating data (i.e. five ~ 170 ks observations and a 56 ks one; Kaspi et al. 2002, hereafter, K02). The mean X-ray luminosity in 2-10 keV is $L_X = 3 \times 10^{43}$ erg s $^{-1}$ (K01 and K02). In addition to a series of ionized absorbers in X-ray, NGC 3783 is also known to exhibit UV absorbers detected with *FUSE* and *HST*/STIS (e.g. Kraemer et al. 2001, and references therein). In particular, K02 conducted an exploratory spectral analysis of the detected X-ray absorbers identifying the physical characteristics of individual ions in the broad-band stacked spectrum assuming phenomenological multiple absorption systems. They did not find any correlation of their velocity shifts or their FWHMs with ionization

potentials. Along similar lines, Krongold et al. (2003) (also Netzer et al. 2003) analyzed the same 900 ks *Chandra* grating spectrum with a self-consistent photoionization model, assuming a simple geometry that consists of a central source emitting an ionizing SED and clouds of gas intercepting our line of sight. Employing `ccloudy` (version 90.04; Ferland et al. 2013) to obtain the individual clouds’ ionization state, they were able to constrain the physical parameters of various ions, i.e. their ionization parameter ξ , column N_H , outflow velocity v and internal turbulent velocity v_{turb} .

In addition to these *Chandra* observations, NGC 3783 was observed with *XMM-Newton*/EPIC over two complete satellite orbits in 2001 (ID 0112210501 and 0112210201) with a total good exposure of 280 ks with gratings (Behar et al. 2003) and ~ 240 ks with CCDs to study the Fe K line profile (Reeves et al. 2004). As a part of their spectral analysis, it was found that the highest ionization component present during this epoch is at an ionization of $\log \xi \simeq 3$ and column density of $N_H \sim 5 \times 10^{22} \text{ cm}^{-2}$ at an estimated distance of $r < 0.1$ pc from the nucleus, while the low ionization states are many pc away. Gabel et al. (2005) confirmed the large distances of the absorbers (with low densities) by observations of C^{+2} transitions from excited levels. More recently, Mehdipour et al. (2017) conducted a *Swift* monitoring campaign triggering joint observations with *XMM-Newton*, *NuSTAR* and *HST*/COS/STIS, in cases of hard *Swift*-XRT spectra, indicating soft X-ray absorption. It was found, in contrast to the previous analyses performed in the 2000-2001 (unobscured) epoch, that the central X-ray region was heavily obscured by outflowing plasma which, besides absorbing the low energy ($E \lesssim 1$ keV) X-rays, exhibited also deep absorption features very distinct from the absorbers detected in the previous UV/X-ray observations. In particular, high-velocity Fe XXV and Fe XXVI absorbers ($v_{\text{out}} \sim$ a few thousand km s^{-1}) of high column density ($N_H \sim 10^{23} \text{ cm}^{-2}$) are clearly present. While comprehensive in their analysis methodology, the physical realization of the series of absorbers observed was still unclear consisting of multiple absorber components as has been often invoked, and the global identification of the observed outflows of many ions is not explicitly revealed.

The presence of ionic species in absorption in the AGN spectra with a broad range in ionization parameter ξ has been generally dealt by considering a number of separate components of well defined ξ . An altogether different (and profitable) approach has been that of Holczer et al. (2007); these authors, noticing the broad range in ξ of the ionic species in the data, assumed a continuous distribution of hydrogen equivalent ionic columns N_H on ξ of the form $N_H \propto \xi^\alpha$ (or more precisely the distribution of $dN_H/d \log \xi$, their so-called Absorption Measure Distribution or AMD as discussed below in equations (1)-(2)). Then, through a minimization procedure, they were able to consolidate the ensemble of the properties of all transitions into the value of single parameter, namely α , which, surprisingly, was found to have a very limited range $\alpha \simeq 0.01 - 0.3$ in the number of AGN with data of sufficiently high quality for such an analysis (Behar 2009, hereafter B09). This behavior has been since found in a joint analysis of twenty six Seyfert outflows (Laha et al. 2014).

While the largest possible location R_{\max} of an absorber can be estimated by $R_{\max} = L_{\text{ion}}/(\xi N_H)$, by recasting the ionization parameter in a slightly different form based on the LoS-integrated hydrogen number density, one can derive a simple analytic expression for a local finite column density ΔN_H for a finite ionization parameter bin $\Delta\xi$ over a small radial LoS extent Δr as

$$\Delta N_H = n(r)\Delta r \propto \xi^{(3-2p)/(p-2)}\Delta\xi, \quad (1)$$

where $n(r) \propto r^{-p}$ is the global wind density profile along a LoS. One can then derive the expected AMD as a function of ξ as

$$\text{AMD} \equiv \lim_{\Delta r \rightarrow 0} \frac{\Delta N_H}{\Delta(\log \xi)} \propto \xi^{-(p-1)/(p-2)}, \quad (2)$$

as similarly derived in B09 and Kazanas et al. (2012). One should note that, for a continuous distribution of N_H on ξ , measurement of N_H of an ion of known ξ provides a measure of its distance r from the ionizing source; repeating this process for ions of a wide range of ξ can then provide the distribution of plasma density $n(r)$ along the observer’s LoS. Thus, the observed slope of AMD implies plasma radial density profiles with a rather limited range in their slopes, namely $1.02 \lesssim p \lesssim 1.22$ (see B09 for 5 Seyfert 1 AGNs including NGC 3783).

Motivated by these considerations we have in the past modeled the AMD observations within the framework of the 2D MHD winds of Contopoulos & Lovelace (1994, hereafter, CL94), generalizations of those of Blandford & Payne (1982, hereafter, BP82), that allow a wider range of wind density profile along the LoS. We found that detailed treatment of the photoionization of MHD winds with $p \simeq 1$ presented a good approximation to the observed AMD dependence and velocity properties of the Seyfert 1’s in the list of B09 (Fukumura et al. 2010a, hereafter, F10a); we also found that reduction of the ionizing X-ray content in the AGN SED, as is appropriate with the BAL QSO spectra, provided velocities consistent with those observed in this AGN class (Fukumura et al. 2010b). Furthermore, considering that our 2D MHD winds are scale invariant (Kazanas et al. 2012), we have applied the same models to the high S/N *Chandra* spectra of the galactic XRB, GRO J1655-40 (Fukumura et al. 2017), to show that our models provide excellent fits to the absorption features (both in absorption depth and in velocity) of the scaled down wind of this stellar black hole. In the context of a mutual interaction between accretion and ejection physics, for example, other groups have also investigated a physical constraint on a global structure of MHD-driven outflows (e.g. Ferreira 1997; Casse & Ferreira 2000a,b; Chakravorty et al. 2016).

In the present work, we employ the same 2D MHD wind model as in our previous works to analyze the 900 ks *Chandra* HETG data of NGC 3783, a well studied, nearby, radio-quiet AGN. With its AMD already determined in B09, our emphasis is the precise determination of the large scale wind parameters, namely the value of the index p , its inclination angle and the wind density normalization. This we do by providing detailed fits

to its most significant absorption lines. In §2 we provide a brief outline of the MHD winds and a comparison with other outflow models. In §3 we describe our analysis procedure. Our results and their comparison to observation are shown in §4 demonstrating that the wind model can describe the observations successfully. We summarize and discuss the implications of the model in §5.

2. Overview of MHD-Driven Wind Model

Given the large bolometric luminosity of AGN and the X-ray contribution to their continua, it is natural to consider radiation pressure (Murray et al. 1995; Proga et al. 2000) and/or X-ray heating (Begelman et al. 1983) as the agents that drive their ubiquitous outflows. While one cannot give a preference to MHD launching over these processes *a priori*, the general argument in favor of the latter and against the simplest versions of the former comes from the form of AMD: For both these processes (i.e. radiation pressure and X-ray heating), at some distance a few times larger than the size of their driving source, these winds will look quasi-spherical, with their velocity increasing with r to its asymptotic value. Then, in their acceleration region ($dv/dr > 0$), due to mass conservation, their densities should decrease faster than r^{-2} resulting in N_H decreasing with increasing ξ (Luketic et al. 2010). Such a behavior is contrary to that observed in the compilation of B09 and Laha et al. (2014). Perhaps more involved models could reproduce the observed $N_H - \xi$ behavior, however, we are not aware of any so far.

On the other hand, the broad range of ξ observed in the data suggests a self-similar process that spans several decades in ξ and r . The 2D winds of BP82 and CL94 serve as a reasonable guess to this end, as they are launched over the entire disk extent. Their velocities (radial and azimuthal) scale with the Keplerian one, $v_{\text{out}} \propto r^{-1/2}$; their densities are separable in r and θ (due to self-similarity) and take the form $n(r, \theta) = n_o(r/r_S)^{-p}f(\theta)$; n_o denotes the density normalization (i.e. wind density at its innermost launching radius on the disk surface at $r \gtrsim r_S$; r_S is the black hole Schwarzschild radius) and it can be expressed in units of dimensionless mass flux rate $\dot{m} = \dot{M}/\dot{M}_{\text{Edd}}$ by

$$n_o \sim \dot{m}/(\sigma_T r_S), \quad (3)$$

where we assume that accreting mass is equally distributed between accretion and outflows at each radius (i.e. $f_w = 1$ as in F10a; Fukumura et al. 2017). The function $f(\theta)$ determines the angular dependence of the wind and it is given by the solution of the Grad-Shafranov equation (see CL94). It has a steep θ -dependence [an approximate expression is $f(\theta) \sim e^{5(\theta-\pi/2)}$, see Fig. 2 of F10a], giving the winds a toroidal appearance. Because of this feature it was suggested (Königl & Kartje 1994) that such winds are in fact the AGN tori invoked to account for AGN unification. The precise form of $f(\theta)$, i.e. the

winds’ opening angle, depends on their specific angular momentum (Fukumura et al. 2014). However, it is qualitatively similar to the form given above.

More importantly, the density radial dependence index p above is intimately related to the AMD shape by equation (2). The wind velocity, mainly in the ϕ -direction as $\theta \rightarrow 90^\circ$, becomes mainly radial at larger latitudes (see Fig. 1a in F10a). Its projection along the observer’s LoS depends on the disk inclination and affects the shape of absorption features; however, due to their Keplerian scaling the outflow velocity component scales with ionization parameter ξ like

$$v_{\text{out}} \propto \xi^{1/\{2(2-p)\}} , \quad (4)$$

a feature that figures prominently in the shapes of the absorption line profiles (see F10a and §4.1).

The winds have the following generic features: (1) The wind structure (i.e. the dependence of N_H on θ and on r/r_S) is fundamentally mass invariant, so they are applicable across the black hole mass scales. (2) They extend from near the black hole ISCO ($r \gtrsim 3r_S$) to the outer disk edge, with velocities that decrease like $r^{-1/2}$. The first feature is indicative of the universal presence of magnetically-launched ionized winds in both AGNs (e.g., Couto et al. 2016; Kraemer et al. 2017 for NGC 4151 and Turner et al. 2005 for NGC 3516) as well as XRBs as often claimed (e.g. Miller et al. 2006, 2008; Kallman et al. 2009; Miller et al. 2015; Fukumura et al. 2017); the second feature clearly points to a strong relevance to the so called ultra-fast outflows (UFOs), increasingly discovered in many Seyfert AGNs (e.g. Reeves et al. 2009; Tombesi et al. 2010, 2013, 2015; Gupta et al. 2015; Gofford et al. 2015) and gravitationally lensed quasars (e.g. Chartas et al. 2009a), and their relation to the lower velocity WAs. Especially, Kraemer et al. (2017) has made a strong argument to support MHD-driven scenario to explain the UFOs detected in NGC 4151 in an approach similar to ours. As noted above, while the wind is present at all radii and their corresponding velocities, its full ionization in the black hole vicinity leaves no absorption imprints in the spectra. These first occur when the wind ionization drops sufficiently to allow the presence of Fe XXVI, Fe XXV; the radii at which these ions first occur depend on the contribution of the ionizing X-rays in the object’s SED. The radii are small in X-ray weak (BAL QSOs) and large in X-ray strong (galactic XRBs) objects, yielding correspondingly large and small velocities for these ions.

The wind photoionization is computed as detailed in F10a, by employing `xstar` (Kallman & Bautista 2001) to determine the plasma ionization and the relevant cross sections to be used in the radiation transfer. Finally, we compute absorption line profiles by calculating photo-excitation cross section

$$\sigma_{\text{abs}} = 0.01495(f_{ij}/\Delta\nu_D)H(a, u) , \quad (5)$$

as a function of local wind velocity $v(r, \theta)$ and its radial shear $\Delta v_{\text{sh}}(r, \theta)$ through the Voigt

function $H(a, u)$, where f_{ij} is the oscillator strength of the transition between the i -th and j -th levels of an ionic species and $\Delta\nu_D$ is the Doppler broadening factor estimated by $\Delta\nu_D \approx (\Delta v_{\text{sh}}/c)\nu_0$ relative to the centroid (rest-frame) frequency ν_0 . With σ_{abs} in equation (5), one can calculate the line depth τ as

$$\tau = \sigma_{\text{abs}} N_{\text{ion}} , \quad (6)$$

where N_{ion} is ionic column density computed with `xstar` calculations (see, e.g. Fukumura et al. 2015). In this formalism, therefore, the line broadening is provided by the natural shear of the wind velocity field and, as such, we eschew the use of the turbulent velocity parameter `vturb`; most importantly, all line profiles are computed using the local values of *the same* global wind parameters rather than being treated as mutually independent multiple gaussian functions, thereby over-constraining our models.

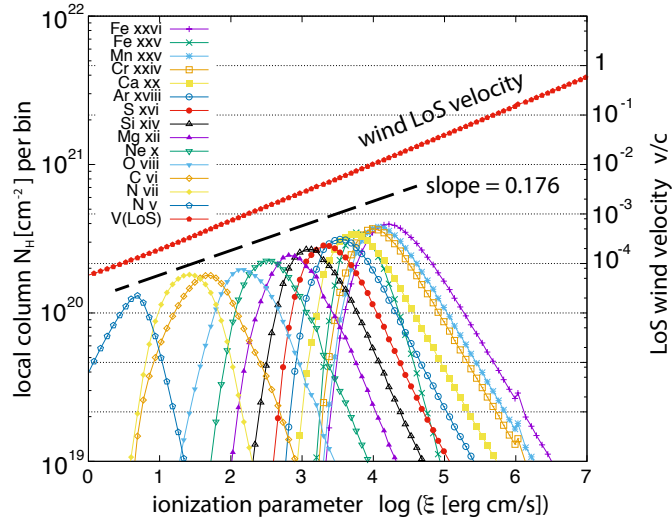


Fig. 1.— An example of synthetic AMD of various ions modeled with the MHD-wind of density profile of $p = 1.15$ for a fiducial set of wind parameters with $\theta = 40^\circ$ and $n_{11} = 13.6$.

3. Analysis

For the present study, we use the 900-ks stacked spectrum from K02 (see their Fig. 5). Our analysis is primarily focused on the $\sim 1 \text{ \AA}$ (Fe) – 20 \AA (O) broad-band spectral fitting with the Galactic absorption of $N_H^{\text{Gal}} = 8.7 \times 10^{20} \text{ cm}^{-2}$ (e.g. Alloin et al. 1995). Closely

following K01 and K02, we estimate the underlying continuum flux in discrete energy bands where no or little line signatures are present (i.e. line-free-zones or LFZs). The continuum spectral shape is assumed to be locally linear instead of a polynomial form, which seems to be quite acceptable, as also claimed in K02, our aim in the present work not being a physical model of the AGN continuum. Contrary to most works which assume a mutually-decoupled, discrete number of ionization and kinematic components to fit groups of lines of similar values of ξ , our models provide a continuum of ionization parameter, column and velocity projection along the LoS with r , the distance from the AGN. As a result, our models are far more constrained with no guarantee that they will provide the correct column (EW) and velocity at the proper values of ξ that support specific ions.

Our investigation begins with calculating the structure of various magnetized wind solutions of different global density profiles that essentially determine the absorber’s AMD. Specifically, we consider $p = 1.29, 1.15, 1, 0.9, 0.8$ and 0.7 consistent with the relevant range obtained in B09 for NGC 3783. For photoionization calculations with `xstar`, we adopt the same ionizing SED of NGC 3783 as determined in K01 (see their Tab. 4) by the LFZ continuum fitting, i.e. a composite spectrum of multiple power-law components of different slopes between 0.2 eV and 30 keV, namely $\Gamma = 2.0$ (0.2 eV - 2 eV), 1.5 (2 eV - 40 eV), 5.77 (40 eV - 0.1 keV) and 1.77 (0.1 keV - 30 keV). We adopt the ionizing luminosity, $L_X = 3 \times 10^{43}$ erg s $^{-1}$, in 1 – 1000 Rydberg (see, e.g., K01 and K02) for photoionization calculations. AGN SED is generally broad-band, covering wavelengths much broader than the X-rays. However, UV photons of energy below 1 Rydberg (13.6 eV, the threshold energy for ionizing hydrogen) do not contribute to photoionization of the wind, while harder X-ray photons of energy higher than 1000 Rydberg (13.6 keV) typically have much lower flux (compared to that of soft X-rays) and do not make a significant impact on the overall photoionization process. The broader disk SED photons emitted near the black hole ($r \gtrsim r_o$) contribute to the cooling of the ionized gas and those have been included in our calculations.

This SED is injected at the coordinate origin as an irradiating source, mimicking the compact point source of an X-ray corona. As mentioned, a given SED will uniquely determine the ionization structure of the wind that “breaks” the otherwise mass-invariant spatial nature of the MHD-driven X-ray absorbers. To show a predictive power of our models, **Figure 1** shows, as one of many (typically 12-15) template calculations, a synthetic AMD for a number of ions computed with $p = 1.15$ wind for $\theta_{\text{obs}} = 40^\circ$ and $n_{11} = 13.6$ where $n_o \equiv n_{11} 10^{11}$ cm $^{-3}$. As seen, the peak column of a given ion increases with ionization parameter ξ (also with decreasing distance r) and the slope of this AMD ($= 0.176$ from eqn. (2); dashed line), consistent with that derived in B09, is set by the wind density slope of $p = 1.15$ assuming the solar abundances. The LoS wind velocity scales as Keplerian, $r^{-1/2}$, in this model.

In our investigation, 18 absorption lines (see **Tables 2-3** and **Figs. 2-3** which will

be discussed later more in §4) are modeled systematically and globally, in the sense that they are all computed within the confines of a single, continuous disk wind; this can pose tight restrictions on the model, since, in such a global model, we cannot afford to adjust individual absorber parameters independently to obtain good fits for specific features. As a result, for a given density distribution p (obtained by spectral fitting and AMD), our model has only two free parameters: (1) The wind density normalization n_o at the innermost launching radius at $r \gtrsim r_S$ on the disk surface and (2) The disk inclination angle θ_{obs} . Elemental abundances could be adjusted individually, but solar abundances are assumed here. Finally, considering that the observed spectrum also exhibits a number of prominent emission lines, especially towards longer wavelengths, we have added, as needed, emission features to our model continuum spectrum of the equivalent width (EW) derived in K02.

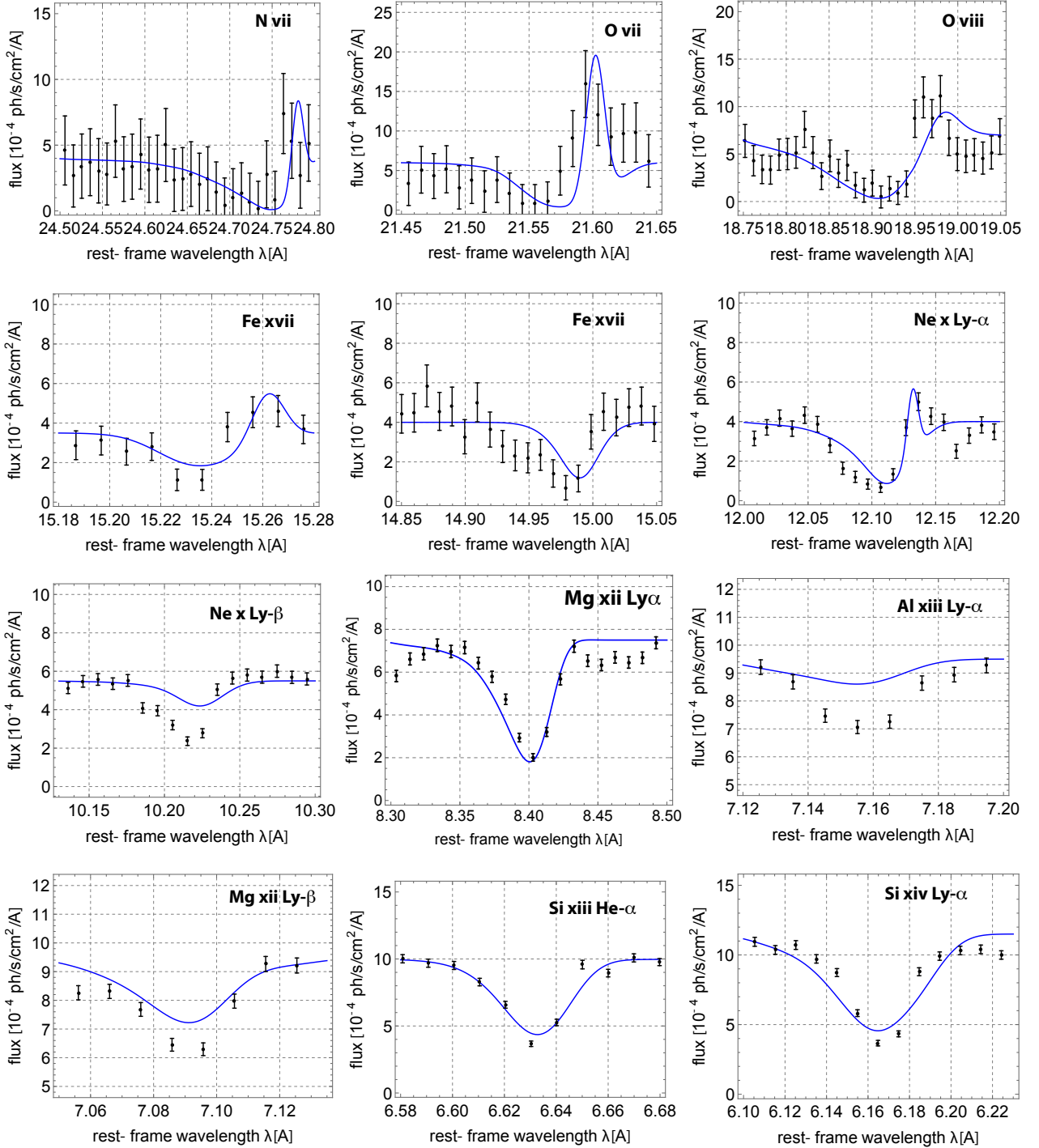


Fig. 2.— Sample of the best-fit spectra calculated from the modeled MHD-wind (in blue lines) with $p = 1.15$, $\theta_{\text{obs}} = 44^\circ$ and $n_{11} = 6.9$. See **Tables 2 and 3** for more details.

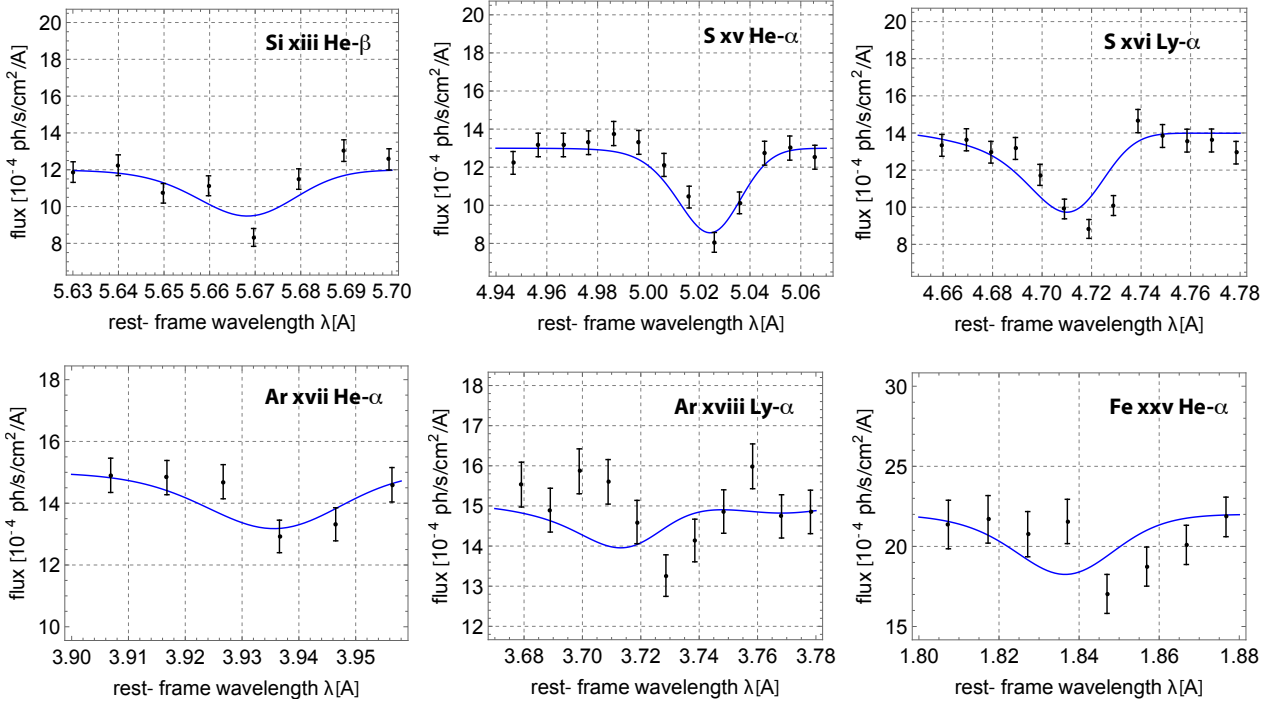


Fig. 3.— Sample of the best-fit spectra calculated from the modeled MHD-wind (in blue lines) with $p = 1.15$, $\theta_{\text{obs}} = 44^\circ$ and $n_{11} = 6.9$. See **Tables 2 and 3** for more details.

Table 1. Primary Grid of MHD-Wind Model Parameters

Primary Parameter	Value
Wind density slope p	0.7, 0.8, 0.9, 1.0, 1.15, 1.29
Inclination angle θ [degrees]	$30^\circ, 40^\circ, 50^\circ$
Wind density normalization n_{11}^\dagger	0.1 - 100

We assume $M = 3 \times 10^7 M_\odot$ (Peterson et al. 2004) and $L_X = 3 \times 10^{43}$ erg s $^{-1}$ (K02).

† Wind density normalization in units of 10^{11} cm $^{-3}$.

First, we try to narrow down an optimal range of the model parameters by crudely exploring the parameter space spanned by $(n_{11}, \theta_{\text{obs}})$ for a series of wind density structure given by p where n_{11} is defined as $n_o \equiv n_{11} 10^{11} \text{ cm}^{-3}$. The likely value of p is successfully constrained within the error set by B09 and by Laha et al. (2014). Following this preliminary investigation, a primary grid of models is determined as shown in **Table 1**. A more thorough analysis is then conducted for these template models to compute in addition the physical parameters of individual ions (e.g. distance r , column N_H , number density n , velocity v_{out} , ionization parameter ξ , plasma temperature T); this is done for the major spectral signatures, i.e. for a total of 18 transition lines from major H/He-like ions; i.e. Fe, Ar, S, Si, Mg, Al, Ne, O and N of relatively large EW found in K02 over the $\sim 1 \text{ \AA} - 20 \text{ \AA}$ band, as they present the most significant indicators of the bestfit global wind solution.

4. Results

To assess quantitatively the model’s statistical significance, we create a large number (typically 12-15) of template wind solutions with different sets of $(n_{11}, \theta_{\text{obs}})$ where $0.1 \leq n_{11} \leq 100$ and $30^\circ \leq \theta_{\text{obs}} \leq 60^\circ$ for a given p within the relevant range inferred from B09, also as shown in **Table 1**. For each such pair of $(n_{11}, \theta_{\text{obs}})$, we compute the predominantly strong absorption line profiles and calculate the χ^2/dof from the ensemble of the 18 absorption lines. Minimization of χ^2 for each density profile yields the bestfit spectrum solution and we calculate the EW for each transition line both from our wind model and data. Besides the value of χ^2 , we also calculate a ratio, as another useful proxy for goodness-of-fit, $R_{\text{EW}} \equiv \text{EW}(\text{obs})/\text{EW}(\text{model})$, of the observed to the model EW for each ion. In **Figure 4** we plot the ratios R_{EW} as a function of atomic number Z along with their mean value \bar{R}_{EW} (shown by red lines). The inset of each panel denotes the resulting value of \bar{R}_{EW} along with the corresponding χ^2/dof values for the specific value of p . Assuming that the wind characteristics vary monotonically with the wind density parameter p , it is implied here that the *global* bestfit solution spanned by the $(n_{11}, \theta_{\text{obs}}; p)$ -space is found somewhere around $p = 1.15$, which is in fact consistent with the result from B09.

To better illustrate the goodness-of-fit in our spectral analysis, we plot in **Figure 5a** the values of $100(\bar{R}_{\text{EW}} - 1)$ (open circles with line) and the corresponding χ^2/dof values (red triangles with line) as a function of the value p . We do see that the χ^2 statistics is rather insensitive to the value of $0.8 \lesssim p \lesssim 1.15$, but increases steeply outside this range. It should be noted here that χ^2 statistics in this dataset is predominantly controlled by a small number of stronger lines with very small error bars produced around $\xi \sim 2.5$. As long as the choice of a pair of $(n_{11}, \theta_{\text{obs}})$ produces the correct value of column density at the given value of ξ , the model gives a similarly small χ^2/dof value. However, it fails here at higher values of ξ because not many high- Z elements are detected with large significance in this

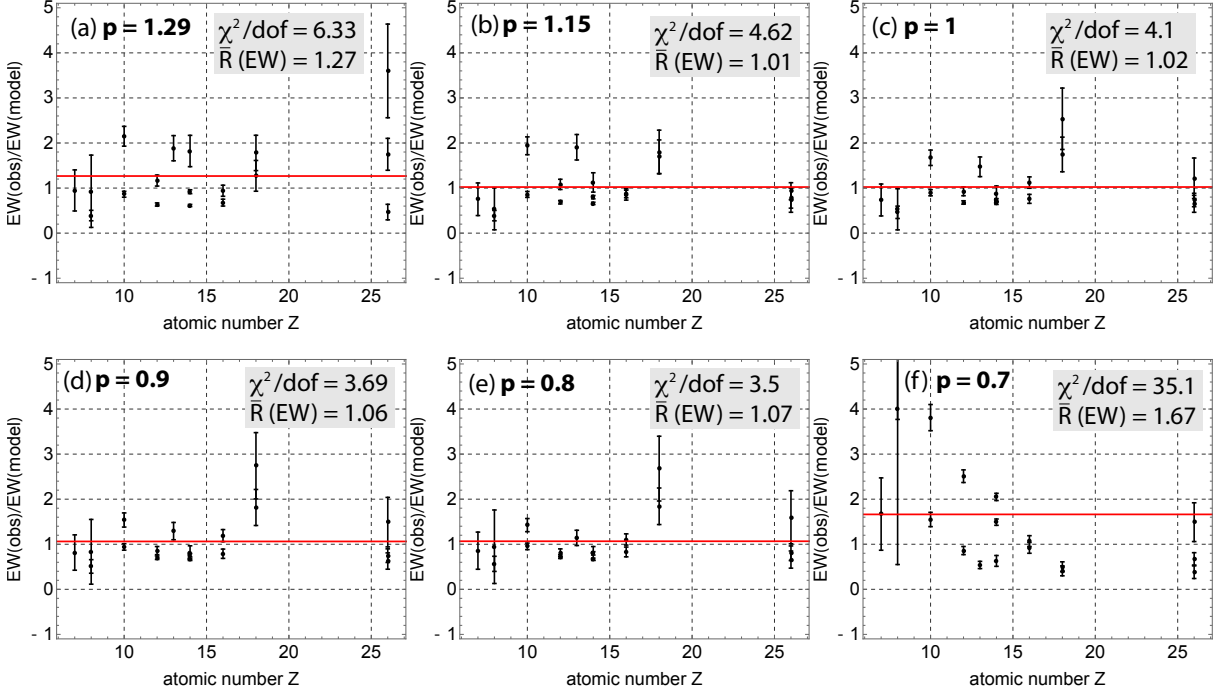


Fig. 4.— EW ratios, $R_{EW} \equiv EW(\text{obs})/EW(\text{model})$, between the model and observation for the same 18 ions shown in **Table 2** derived from the bestfit models for various wind density profiles; (a) $p = 1.29$, (b) 1.15, (c) 1.0, (d) 0.9, (e) 0.8 and (f) 0.7 along with its *mean* value, \bar{R}_{EW} , (shown in red lines). Also shown are the derived χ^2/dof values for each bestfit model from 18 ions in **Table 2**. As seen, the $p = 1.0 - 1.15$ wind is physically more favored at a statistically significant level.

data. On the other hand, the EW ratios \bar{R}_{EW} fare better in that respect, as they provide an alternative to the AMD covering a larger ξ -range. From the combination of the two proxies here, we see again that p in the range $\sim 1 - 1.15$ provides the most satisfactory fit to the data. The most likely range from our bestfit (labeled as *MHD Wind*) and the AMD in B09 (labeled as *AMD*) are respectively denoted by shaded regions. In the remainder of this paper, therefore, we choose the value $p = 1.15$ as the bestfit wind solution from a global perspective. For $p = 1.15$, we also present in **Figure 5b** a contour map of χ^2/dof (color-coded as shown) in the $\theta_{\text{obs}} - n_{11}$ plane to obtain the bestfit solution of $\theta \simeq 44^\circ$ and $n_{11} \simeq 6.9$ (denoted by cross).

Focused on the obtained global bestfit solution, we have presented earlier in **Figures 2-**

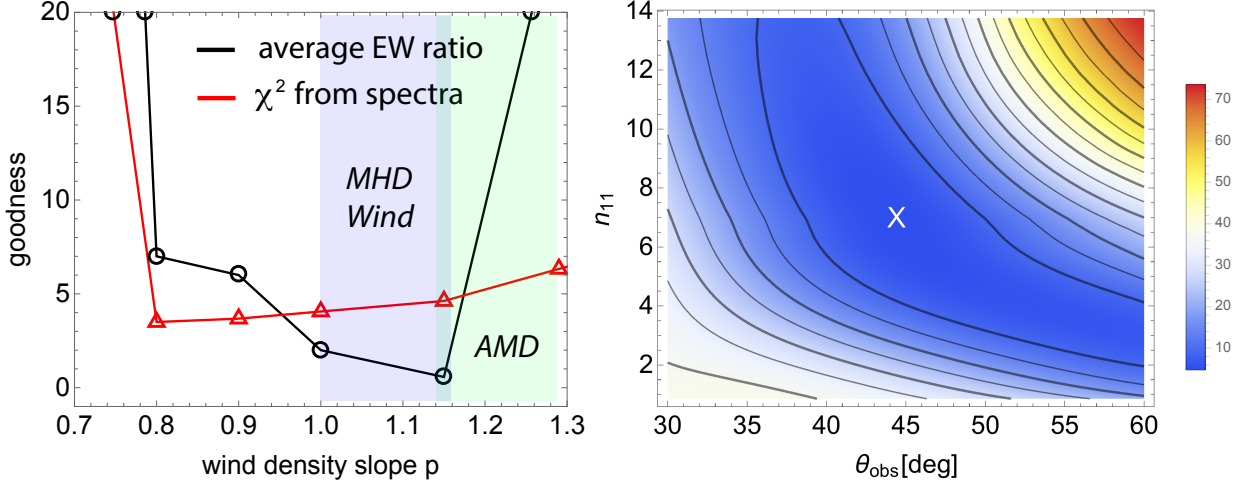


Fig. 5.— (a) Goodness-of-fit assessed by χ^2 -statistics (red triangles) and the *mean* EW ratios (dark circles), $\bar{R}_{\text{EW}} \equiv 100(\bar{R}-1)$, i.e. its % deviation from a perfect match, corresponding to **Figure 4** for different density slope p considered in this work. The light blue band indicates the most likely values based on the combination of the two constraints. Note that the points for $p = 0.7$ are off the range as similarly shown in **Figure 4**. The most likely range from our bestfit (labeled as *MHD Wind*) and the AMD in B09 (labeled as *AMD*) are respectively denoted by shaded regions. (b) A contour plot of χ^2/dof values (color-coded) corresponding to the model parameters $(n_{11}, \theta_{\text{obs}})$ from the $p = 1.15$ wind with its bestfit solution $\theta = 44^\circ$ and $n_{11} = 6.9$ (white X).

3 the bestfit profiles of the 18 lines of **Table 2** with $p = 1.15$, $\theta_{\text{obs}} = 44^\circ$ and $n_{11} = 6.9$ (i.e. $n_o = 6.9 \times 10^{11} \text{ cm}^{-3}$) overlaid on the data. Note that our spectral calculations employ the Voigt profile as described above, with the wind shear as the only line broadening process, eschewing the use of an artificial turbulent velocity, customarily employed in similar analyses. This set of wind parameters is statistically favored among the models considered here (as demonstrated in **Fig. 5**). As also seen in **Figures 2 and 3**, the global bestfit model (i.e. $p = 1.15$ wind) is generally consistent with most significant absorber transitions, both in line depth and shape (the Ne x Ly β feature may involve line blending, not considered here). As discussed elsewhere in this paper, the Fe xxv He α line, typically strong in the AGN absorption spectra (Tombesi et al. 2013), is rather weak in this object, in agreement with our model, lending additional support to it.

Table 2. Line Measurements and Bestfit Model for 18 Absorbers

#	Ion	Wavelength [†]	EW(mod) [‡]	EW(obs) [‡]	$v_{\text{out}}^{\text{obs}}/v_{\text{out}}^{\text{mod}}$ Δ	EW(obs)/EW(mod)
1	Fe xxv He α	1.8505	5.18	3.8 ± 1.4	571/2,187	0.73 ± 0.27
2	Ar xviii Ly α	3.7310	2.28	4.1 ± 1.1	192/1,446	1.8 ± 0.48
3	Ar xvii He α	3.9493	2.94	5.0 ± 1.1	965/1,009	1.69 ± 0.37
4	S xvi Ly α	4.7274	12.1	10.7 ± 1.2	536/1,103	0.88 ± 0.09
5	S xv He α	5.0387	10.9	9.2 ± 1.2	759/874	0.84 ± 0.11
6	Si xiii He β	5.6807	5.59	6.30 ± 1.2	582/670	1.12 ± 0.21
7	Si xiv Ly α	6.1804	31.0	20.5 ± 0.8	755/747	0.66 ± 0.025
8	Si xiii He α	6.6480	18.6	14.9 ± 0.7	798/676	0.79 ± 0.04
9	Mg xii Ly β	7.1058	7.95	8.60 ± 0.9	424/624	1.1 ± 0.11
10	Al xiii Ly α	7.1763	2.83	5.4 ± 0.8	883/890	1.9 ± 0.28
11	Mg xii Ly α	8.4192	36.6	25.1 ± 1.4	577/683	0.69 ± 0.04
12	Ne x Ly β	10.238	10.1	19.6 ± 2.0	664/439	1.9 ± 0.19
13	Ne x Ly α	12.132	44.3	38.1 ± 2.9	622/494	0.86 ± 0.065
14	Fe xvii	15.014	28.2	26.2 ± 5.3	623/399	0.93 ± 0.18
15	Fe xvii	15.262	19.1	14.9 ± 4.3	699/510	0.78 ± 0.22
16	O viii Ly α	18.969	137	53.6 ± 15.9	925/742	0.38 ± 0.11
17	O vii He α	21.602	74.1	40.1 ± 34.6	629/333	0.54 ± 0.46
18	N vii Ly α	24.781	96.5	72.6 ± 34.9	573/387	0.75 ± 0.36

[†] In units of \AA .

[‡] In units of m\AA taken from Kaspi et al. (2002).

Δ Velocities in units of km s^{-1} .

Besides the observable quantities discussed so far (as listed in **Table 2**), we also calculate the characteristics associated with specific lines of our magnetically-driven disk-winds. Representative wind variables are listed in **Table 3** in order of increasing characteristic LoS distance, r_c , (second column) where the local ionic column obtains its maximum value for each line. We also show the local wind density n_c (fifth column) and line optical depth τ_c (seventh column) at this characteristic radius r_c . Accordingly, we keep track of the radial dynamic range over which the local ionic column stays within 50% of its maximum value. Within this range, the ionization parameter ξ (third column) and the wind temperature T (fourth column) are computed as well. Lastly, the LoS-integrated hydrogen equivalent column density of each ion N_H^{tot} is also calculated (sixth column). As shown, the distances of absorbers range from 0.2 pc to 30 pc scales in X-rays, exactly as estimated for this source by Reeves et al. (2004), Behar et al. (2003) and Gabel et al. (2005). In most of the radial extent of the wind, absorbers are optically thin where the radiative transfer calculations with `xstar` are justified.

It should be reminded that continuous outflows are characterized, in general, by a gradient of the wind’s physical quantities (e.g.density, velocity etc.), a situation fundamentally distinct from outflow models consisting of distinct, independent, multiple kinematic and ionization components. In the continuous outflow situation all wind elements leave their imprint on the line profile at their respective velocities, weighted of course by the corresponding ionic abundance. For example, in the specific wind structure considered here, the ionic abundances are not symmetric with respect to the value of ξ where they achieve their maximum: they fall much sharper at lower ξ -values (and lower velocities) than at higher ones (higher velocities) (see one of the template AMDs as shown in **Fig. 1**). As a result, the resulting absorption lines are asymmetric, skewed toward their blue side and their peak absorption is at a velocity larger than that corresponding to their peak column (see §4.1 below).

Table 3. Bestfit Photoionization Modeling for 18 Absorbers

#	Ion	$\log(r_c/r_S)^\dagger$	$\Delta(\log \xi)^\ddagger$	$\Delta(\log T)^\diamond$	$\log n_c^\#$	$N_H^{\text{tot}\Delta}$	τ_c
1	Fe xxv He α	4.96	3.5 - 4.2	6.0 - 6.4	6.1	6.1	0.27
2	Ar xviii Ly α	5.2	3.0 - 4.1	5.9 - 6.3	5.8	9.5	0.048
3	Ar xvii He α	6.7	2.7 - 3.5	5.8 - 6.0	5.4	5.7	0.22
4	S xvi Ly α	5.5	2.8 - 3.9	5.8 - 6.2	5.5	8.7	0.27
5	S xv He α	6.0	2.5 - 3.3	5.7 - 5.9	4.9	4.6	0.12
6	Si xiii He β	6.3	2.2 - 2.9	5.6 - 5.8	4.5	4.1	0.76
7	Si xiv Ly α	5.8	2.5 - 3.7	5.7 - 6.1	5.1	8.1	1.0
8	Si xiii He α	6.4	2.2 - 3.0	5.6 - 5.9	4.5	4.0	4.4
9	Mg xii Ly β	6.1	2.3 - 3.4	5.6 - 6.0	4.8	4.8	0.27
10	Al xiii Ly α	6.1	2.3 - 3.4	5.6 - 6.0	4.8	6.7	0.05
11	Mg xii Ly α	6.1	2.3 - 3.4	5.6 - 6.0	4.8	4.8	1.7
12	Ne x Ly β	6.5	2.0 - 3.0	5.0 - 5.8	4.3	4.9	0.38
13	Ne x Ly α	6.5	2.0 - 3.0	5.0 - 5.8	4.3	4.9	2.4
14	Fe xvii	6.6	2.1 - 2.6	5.5 - 5.7	4.2	1.3	18
15	Fe xvii	6.6	2.1 - 2.6	5.5 - 5.7	4.2	1.3	4.5
16	O viii Ly α	6.9	1.6 - 2.6	4.6 - 5.7	3.8	4.3	100
17	O vii He α	7.4	1.2 - 1.6	4.4 - 4.8	3.3	3.9	547
18	N vii Ly α	7.1	1.4 - 2.2	4.5 - 5.6	3.6	4.3	13

[†] Characteristic LoS distance r_c where the modeled AMD of specific charge state becomes maximum (i.e. $\Delta N_H/\Delta(\log \xi)$ is maximum). See the text for details.

[‡] Range of ionization parameter ξ [erg cm s⁻¹] over which the local ionic column per ionization parameter bin is greater than 50% of the locally maximum ionic column.

[◇] Range of temperature T [K] over which the local ionic column per ionization parameter bin is greater than 50% of the locally maximum ionic column.

[‡] Characteristic number density n_c [cm⁻³] of ion at $r = r_c$.

[△] LoS-integrated column N_H^{tot} [$\times 10^{21}$ cm⁻²] of ion .

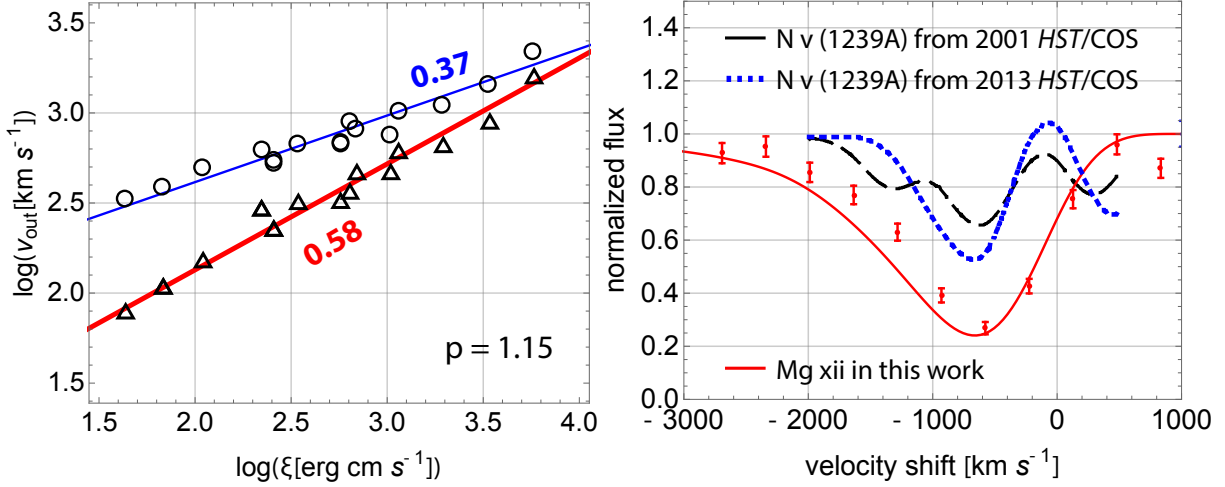


Fig. 6.— (a) The observed correlation between the LoS outflow speed v_{out} [km s $^{-1}$] and ionization parameter ξ [erg cm s $^{-1}$] for the same 18 ions in **Tables 2-3**. Triangles denote a correlation with the velocity at which the ionic column derived from our model is locally maximum for each ion, while circles show a correlation for the same ions when the velocity is simply determined by the trough of the bestfit spectrum model for each ion in **Figures 2-3**. The blue line denotes the corresponding linear regression of slope 0.37 for the circles. Note that the predicted scaling (in red) from equation (4), $v_{\text{out}} \propto \xi^{1/\{2(2-p)\}} = \xi^{0.58}$ for $p = 1.15$, agrees very well with the bestfit correlation (triangles). (b) The solid red curve shows the normalized velocity profile of Mg xii Ly α (8.4192 Å; red) of the bestfit model $p = 1.15$ wind of this work. The dashed (dark) and dotted (blue) curves respectively represent the profiles of the UV N v absorber (1239 Å) from *HST*/COS 2001 and 2013 observations in Scott et al. (2014). The UV spectra are intentionally smoothed to the velocity resolution (~ 100 km s $^{-1}$) of *Chandra*/HETG for comparison.

4.1. The $v_{\text{out}} - \xi$ Correlation

The continuous variation of ξ and outflow velocity v_{out} with distance r implies a correlation between ξ and the projected outflow velocity along the observer’s LoS v_{out} (i.e. eqn. (4)). Such a relation has been searched empirically in the data. For example, Detmers et al. (2011) found the correlation $v_{\text{out}} \propto \xi^{0.64 \pm 0.1}$ in the data of the 600-ks *XMM-Newton*/RGS multiwavelength campaign of Mrk 509 roughly consistent with our scaling value in Eq. (3) for $p = 1.15$. Tombesi et al. (2013) has conducted a systematic analysis on the observed WAs and UFOs from a sample of 35 Seyfert 1 galaxies and found that $v_{\text{out}} \propto \xi^{0.65}$ for the WAs and UFOs combined together, while $v_{\text{out}} \propto \xi^{0.31}$ for the WAs only (see also Laha et al. 2014 for a similar analysis).

However, before strong conclusions are drawn, one should first bear in mind that all the points shown in Tombesi et al. (2013) represent data from a large number of AGN of different inclinations, columns and SEDs. The derived scaling law, equation (4), appears to be generic, but it should be reminded (as mentioned elsewhere in this paper) that the magnetic field and velocity structure of our model winds are self-similar, laterally stacked paraboloids, while the ionizing radiation (at least in our calculations so far) is spherically symmetric about the AGN. Therefore, deviations from the generic relation of equation (4) should not be surprising in a more detailed modeling.

Figure 6a depicts such $v_{\text{out}} - \xi$ correlations based on two different standpoints. The triangles represent the correlation of ion velocity v_{out} with the value of ξ at a characteristic radius, r_c (see **Table 3**), where each ion achieves its maximum column density by photoionization along the LoS (see **Fig. 1**); these points are indeed in excellent agreement with the expected relation of equation (4) of slope of 0.58 (depicted by red line) for the bestfit $p = 1.15$ wind. However, the line optical depth τ_{ion} may not necessarily be the greatest at $r = r_c$, as the photo-absorption cross section σ_{abs} given by equation (5) is monotonically increasing with distance causing the peak of the line depth to shift slightly outwards along the LoS. Hence, the outflow velocity derived from the model spectral line trough is systematically lower than the velocity at $r = r_c$; however this shift cannot be deduced without detailed line modeling. Thus, as is customary, we use a centroid wavelength to refer to the wind LoS velocity. The results of these measurements based on the line troughs are represented by the circles in Figure 6a; as already seen in Figures 2 and 3, these data agree well with the expected velocities from the best-fit model. Their velocities appear to be well correlated to the ionization parameter ξ , but its slope is different from the simple analytic prediction of $v_{\text{out}} \propto \xi^{1/\{2(2-p)\}}$. The best-fit linear regression yields $v_{\text{out}} \propto \xi^{0.37}$ (denoted by blue line). This is in fact very close to that from the WA ($\simeq 0.31$) quoted in Tombesi et al. (2013). One cannot fail to notice that this is much flatter than the one would naively expect from equation (4).

In summary, one should note that detailed modeling of the line profiles of individual

objects are necessary, along the lines of a well defined model, in order to decide on the implications of the $v_{\text{out}} - \xi$ correlations of specific observations. We defer general statements on this issue until we have modeled this correlation for a wide range of wind parameters, the subject of a future publication. Finally, one should bear in mind that our models represent a self-similar *steady-state* model. We do know that AGN are variable, both on short and long time scales. Our models assume that variations in the disk mass flux are also reflected in mass flux of the wind; these variations are likely to break the simple power law density profiles assumed so far, producing, for example, increased absorption in earlier less absorbed spectra (e.g. Mehdipour et al. 2017). Also, factors other than magnetic fields may influence the wind mass flux; for example, increased mass flux beyond that of self similarity at the inner wind regions due, e.g. to radiation pressure, would produce higher columns for the highest ξ ions, in agreement with the Tombesi et al. (2013) compilation.

5. Discussion & Conclusions

The 900-ks *Chandra*/HETG spectrum of the luminous, radio-quiet Seyfert 1 AGN, NGC 3783, is analyzed with emphasis on its X-ray absorption spectrum which was modeled within the framework of magnetically-driven accretion-disk winds. With its AMD already determined in B09, in conjunction with earlier extensive spectral studies (e.g. K01, K02 and Krongold et al. 2003), we focused on the $\sim 2 \text{ \AA} - 20 \text{ \AA}$ X-ray band to model the properties of its most important transitions in this range. Comparison of the absorber properties to observation, then, provides the global parameters of this wind, namely its density index p , its normalization n_o at its innermost launch radius (of order r_S) and its inclination angle θ_{obs} . Thus we found, in the context of this model, that the wind radial density profile is given by $n(r) \simeq 6.9 \times 10^{11} (r/r_S)^{-1.15} \text{ cm}^{-3}$, along with $\theta \simeq 44^\circ$ for the inclination angle. One should note that the value of the density profile index $p = 1.15$ is consistent with that inferred in B09 obtained on the basis of the apparent absorption line column N_H . However, the present analysis includes additional kinematic information (see **Figs. 2-3**) via mutually coupled ions that affects the shape and EW of the observed lines, features that allow for a refinement of the precise value for p . The obtained values of (p, n_{11}) as well as the inclination angle θ_{obs} are determined by fitting the spectroscopic observations assuming a radially self-similar wind model. These constraints are therefore consistent and reasonable with the spectral results.

This is our second application of the specific MHD wind formalism to determine their global properties through modeling the multi-line absorption X-ray spectra of accreting black holes, our previous analysis being that of the spectrum of the galactic X-ray black hole binary GRO J1655-40 (Fukumura et al. 2017). We have argued elsewhere (e.g. Kazanas et al. 2012) that these models are scale-free and should be applicable to any accreting black holes. We are very encouraged by the ability of this most simple, self-similar, model to reproduce the properties of absorption features of outflows associated with objects of such disparate mass scales. In this section we discuss the results and conclusions of our present analysis and their relation to similar observations of this and other AGNs.

In fact, it has been long speculated that some Seyfert AGNs may exhibit ionized winds whose physical characteristics indeed favors for MHD-driven scenario. For example, Turner et al. (2005) found a series of X-ray absorption lines in *Chandra* grating data and investigated the nature of their physical properties. They argue that some absorbers are too highly ionized to be radiatively accelerated, which can be a circumstantial evidence for a hydromagnetic origin for the outflow in NGC 3516. From a synergistic analysis of another well-known Seyfert 1 galaxy, NGC 4151, by Couto et al. (2016), some components of the observed X-ray absorbers are highly ionized. Given the observed 2-10 keV flux and photoionization modeling, the calculated force multiplier is found to be too small to drive the observed winds, perhaps indicating a magnetic-origin. These observations may be

pointing to the relevance of MHD-driven process at least in part if not fully, as discussed in this work for NGC 3783 as well as our earlier work for the XRB, GRO J1655-40.

It should be noted that our model treats the underlying accretion disk as a boundary condition that provides the seed plasma for the winds. Hence, accretion and outflows are solved independently. In reality, however, the inflow-outflow problem must be self-consistently considered. Some authors (e.g. Ferreira 1997; Casse & Ferreira 2000a,b; Chakravorty et al. 2016) have attempted this problem by assuming that magnetic flux is brought in from infinity and its advection is balanced by its diffusion. They show that this requirement tends to lead to a very steep density profile of $p \simeq 3/2$ inconsistent with the X-ray AMD observations (e.g. B09), as discussed in this paper. Under a certain ionization parameter space, on the other hand, they argue that a less steep profile ($p \sim 1.1$), as favored in our work here, could be obtained. The qualitative argument for winds such as considered here is that the viscous torques that transfer outward the disk angular momentum transfer also mechanical energy (and possibly magnetic flux; see Contopoulos 2017). It is this energy that powers the wind mass flux. Although the mutual coupling among inflows, outflows and threaded magnetic fields is fundamentally important, it is beyond the scope of our current work.

Among the X-ray AGN absorption features, Fe XXV and Fe XXVI have attracted particular attention because of their ubiquity and high velocities as in the UFOs (Tombesi et al. 2013). These properties have prompted their study in NGC 3783 also by *XMM-Newton* (Reeves et al. 2004). Fits of the broader Fe XXV band with multi-component, photoionized plasma provide absorber parameters similar to ours. However, in similarity with Mrk 509, the Fe XXV feature is weak in this AGN too. We speculate that this is the result of the relatively low inclination angle and the SEDs in both objects. While systematically consistent for many ions, the observed velocities of high-Z ions, such as Fe and Ar, appear to be lower than what is predicted by the model (i.e. $\sim 1,000 - 2,000 \text{ km s}^{-1}$; see Table 2 and Fig. 3). As the characteristic of the wind model, heavier absorbers (e.g. Fe) emerge at smaller distances where the velocities are higher. As a consequence, the resulting absorption features are expected to be broader. There are several ways to account for the discrepancy that may involve all of them; First of all, the error bars of these line transitions are much larger than those of longer wavelengths making this discrepancy less significant. Secondly, our calculations have ignored scattering which may fill in some of the line profiles (note that this would occur preferentially at the shorter wavelengths of the profiles as the scattering depth is larger at smaller distances and the scattering cross section competes with that of photoabsorption). Finally, break-down of self-similarity near the axis at small radii and/or of the smoothness of the wind geometry may also contribute to this discrepancy. While beyond the scope of the current paper, we plan to address this issue quantitatively in a future work.

An important set of observations additional to those discussed herein have been those

of Mehdipour et al. (2017), who analyzed the multiwavelength spectra of NGC 3783 during a recent, reduced soft X-ray ($E \lesssim 1$ keV) flux state in order to study the properties and physics of obscuring plasma in this AGN. They found that obscuration of the X-rays at $E \lesssim 1$ keV produced also more prominent Fe xxvi and Fe xxv absorption. They interpreted their results as due to the effects of an intervening, highly ionized obscurer. We defer detailed analysis of this latest data to a future publication. However, we would like to point out that within our framework there may be a natural explanation, considering that increased absorption column is due to increased *poloidal mass flux*. Such a view is supported by the fact that the optical and UV (O-UV) continua of their 2016 observations are a factor of $\simeq 2$ higher than that of the early 2000’s ones (the so-called “unobscured state”) analyzed in the present paper (while their hard X-ray fluxes have so far remained unchanged). If the wind and disk mass fluxes vary in unison, as implicit in our model, the excess mass flux of the absorber (i.e. the wind) is then related to increased mass flux in the disk that drives the O-UV emission of this object. If the O-UV spectrum is emitted at radii larger than those of the X-rays (Chartas et al. 2009b; Kazanas 2015) and the excess mass is slowly being accreted inward, one should expect an increase in the X-ray flux to follow that of the O-UV, with corresponding increase in soft X-ray ionization.

5.1. Mass-Accretion for Disk-Winds

Our wind model predicts that the wind mass flux scales with distance as $\dot{M}(x) \propto x^{3/2-p}$ where $x \equiv r/r_o \sim r/r_S$. This means that, for $p < 3/2$, the wind mass flux increases with distance; i.e. most of the mass available for accretion is lost into the wind at large distances from the black hole. This implies that the disk accretion rate should decrease toward the black hole. While our models do not address this problem, they have to allow for accretion onto the black hole at a rate sufficient to produce the observed bolometric luminosity. To provide an approximate resolution of this issue, we assume that the ratio of the wind mass flux to that of the disk is unity, $f_w \simeq 1$, independent of the radius (see F10a; Fukumura et al. 2017). In this way, we can connect the mass flux at the outer edge of the disk¹ to that producing the observed luminosity through accretion onto the black hole. This argument then implies

$$\dot{M}(x = x_{\max} \simeq 10^6) \sim 10^{3(3-2p)} \dot{M}(x = 1) , \quad (7)$$

where $\dot{M}(x = 1) \simeq n_o \sigma_T r_S \dot{M}_E$ is given in terms of the wind density normalization n_o with $\dot{M}_E \equiv L_E/c^2$ being the Eddington mass-flux rate, L_E being the Eddington luminosity and

¹This part of the wind may be viewed as the putative torus in the context of a unified torus scenario (e.g. Königl & Kartje 1994; Kazanas et al. 2012).

σ_T being the Thomson cross section. For our bestfit model with $p = 1.15$ and $n_{11} = 6.9$ and for a black hole mass $M = 3 \times 10^7 M_\odot$, one obtains

$$\dot{M}(x \simeq 1) \sim 4\dot{M}_E \simeq 1.8 \times 10^{27} \text{ g s}^{-1}, \quad (8)$$

$$\dot{M}(x_{\text{max}} \simeq 10^6) \sim 500\dot{M}_E \simeq 2.2 \times 10^{29} \text{ g s}^{-1}, \quad (9)$$

where $\dot{M}(x_{\text{max}} \simeq 10^6)$ is available over an extended region ($x \lesssim 10^6$) of the disk to be provided for winds. Liberated accretion power via gravitational potential energy, given by $L \propto GM\dot{M}/r \propto x^{1/2-p}$, is more significant at *smaller* distances contrary to the dominant mass-accretion rate \dot{M} at *larger* radii in equation (7). Similarly, wind kinetic luminosity scales as

$$L_{\text{wind}} \sim \dot{M}v_{\text{out}}^2 \propto x^{1/2-p}, \quad (10)$$

and hence this power is very small ($\simeq 10^{-4}$) at $x_{\text{max}} \simeq 10^6$ for $p = 1.15$, despite its large mass flux there, compared to that carried onto the black hole at $x \sim 1$. This fact has also been noted by Kraemer & Crenshaw (2012) which, using UV photonization considerations for 7 Seyfert galaxies including NGC 3783, estimated that the UV absorber’s mass flux is ~ 100 times larger than that is needed to power the observed luminosity by accretion onto the black hole in consistence with our finding.

The bestfit value of $n_{11} = 6.9$ we have obtained implies Thomson depth of order $\gtrsim 1$ at the wind’s innermost radius. For $f_w \simeq 1$, the corresponding accretion kinetic luminosity is $\sim 10^{46} \text{ erg s}^{-1}$ (proportionally smaller for a smaller black hole mass), and considering the efficiency of a Schwarzschild black hole ($\eta \simeq 0.05$, and maybe a little smaller if radiation is trapped in the flow), we obtain a bolometric luminosity of $\sim 5 \times 10^{44} \text{ erg s}^{-1}$; considering its apportionment across the entire electromagnetic spectrum, the ionizing luminosity of $L_X \sim 3 \times 10^{43} \text{ erg s}^{-1}$ employed in our modeling seems to be in a reasonable agreement with the model’s global mass flux budget and observations (see, e.g., Fig. 6 in Mehdipour et al. 2017).

5.2. Physical Link: UV/X-ray Absorbers and NLR Outflows

One of the open issues regarding AGN winds is the link between their X-ray absorbers with the known UV absorbers (e.g. C IV and N V) found in *HST*/COS/STIS observations (e.g. Crenshaw et al. 1999; Crenshaw, Kraemer & George 2003; Crenshaw & Kraemer 2012). Despite a number of analyses supporting this relation to date (Mathur et al. 1994, 1995; Crenshaw et al. 1999; Collinge et al. 2001; Kraemer et al. 2002; Crenshaw, Kraemer & George 2003; Krongold et al. 2003; Kaastra et al. 2014), an explicit physical description of the underlying plasma dynamics is missing.

The simultaneous presence of *HST*, *Chandra* and *XMM-Newton* in orbit has provided the opportunity of the synergistic study of absorbers in the X-ray and UV regions of the spectra of several AGNs. For example, Collinge et al. (2001) showed that the lower ionization, X-ray Fe absorption features of NGC 4051 had corresponding UV counterparts, while the higher-ionization, higher-velocity X-ray absorbers of the spectrum lacked an equivalent UV absorption, indicating the absence of these ions in the higher ionization, higher velocity plasma. With respect to NGC 3783, Gabel et al. (2003) found the UV absorption features to have velocity structures similar to their X-ray counterparts, thereby arguing for the continuity of both absorption components.

In **Figure 6b**, we show the data and our model profile of the Mg XII line (solid red), overlaid on the observed absorption lines of N V (dashed dark for 2001 data and dotted blue for 2013 data) obtained by *HST*/COS data (from Scott et al. 2014; see their Fig. 9) smoothed to the *Chandra*/HETG resolution ($\sim 100 \text{ km s}^{-1}$) for fair comparison. It is interesting that both UV and X-ray lines exhibit approximately the *same velocity structure* (i.e. trough position and width) and the *same absorption depth* ($\tau_{\text{N V}} \simeq 0.45$, $\tau_{\text{Mg XII}} \simeq 1.5$) considering the difference in ionic columns produced. It is noted that 2001 UV N V line appears to exhibit a multiple trough feature. As discussed in Scott et al. (2014), it is conceivable that poorer spectral (velocity) resolution of X-ray measurements with *Chandra*/HETG may limit a detection of finer (smaller) kinematic components of X-ray absorbers. Nonetheless, the overall kinematic component seen in both UV (N V) and X-ray (Mg XII) observations looks surprisingly similar in depth and broadness in general. Since our model is focused primarily on X-ray winds, we will not discuss the UV absorbers any further. This would generally be an unlikely situation, because the two lines “live” in very different regions in ξ -space (of $\log \xi \simeq 1$ for N V and $\log \xi \simeq 2 - 3$ for Mg XII, respectively) and the N V has much higher absorption cross section. One could consider that their similar velocity structure argues for these ions belonging to the asymptotic velocity (and also asymptotic ξ) region of a spherically symmetric wind whose mass flux can be arranged so that the ionic abundances of these two ions are roughly inversely proportional to their cross sections; this would produce similar line kinematics and depths. However, such a wind would preclude the presence of higher- ξ , higher- v_{out} ions such as Fe XXVI.

On the other hand, a UV/X-ray absorption line similarity is possible within our model if we assume that the wind terminates at a distance r , or equivalently, at an ionization parameter ξ , where N V is still subdominant such that the ion abundances of these two ions are roughly inversely proportional to their cross section (since the N V column is smaller than that of Mg XII, these are only broad estimates); then, their similar profiles will reflect the kinematic properties of this zone while maintaining roughly similar depths.

We have extended our X-ray ionization calculations to the UV ionization zone of N V to find a line absorption depth $\tau_{\text{N V}} \simeq 0.35$ at $r/r_S \sim 10^6$ and $v_{\text{out}} \sim 500 \text{ km s}^{-1}$. The termination of the wind takes place in our model at a distance of $\sim 1 \text{ pc}$ along the LoS.

An extension of the (self-similar) wind to larger distances would result in much lower $N v$ velocity and high absorption $N v$ depth that are not observed. Finally, one additional consideration in comparing the O-UV and X-ray absorption line profiles is that the UV source region is likely to be larger than that of the X-rays (Chartas et al. 2009b); therefore their profiles do not necessarily correspond to the same LoS and velocity structures. Also, the UV source may not be totally covered by the wind if it is clumpy.

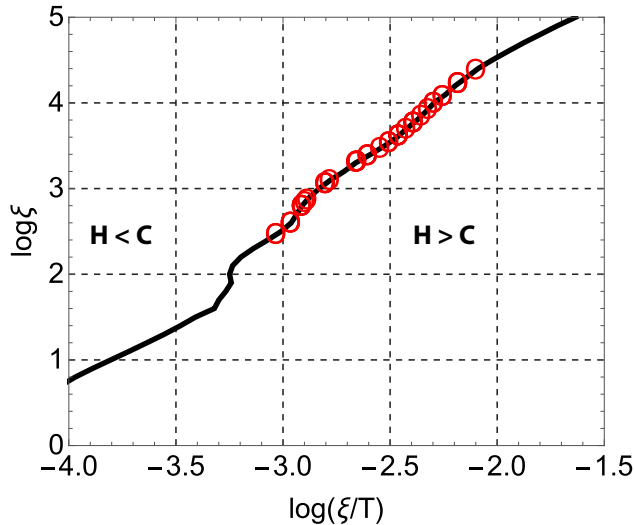


Fig. 7.— Modeled cooling curve (in black) derived from the photoionization calculation with the bestfit wind solution of $p = 1.15$. Circles (in red) indicate the positions of 18 absorbers listed in **Tables 2-3** in the parameter space. Regions where heating (H) or cooling (C) dominates are also indicated.

5.3. Clumpy Absorbers

An altogether different scenario to produce the observed AMD distribution is that of AGN clouds (clouds have been a basic staple of AGN phenomenology, especially since the work of Krolik et al. 1981) that are not uniform but include a density stratification (e.g. Gonçalves et al. 2006; Rózańska et al. 2006; Adhikari et al. 2015; Stern et al. 2014; Goosmann et al. 2016). This alternative view is mostly prompted by lacking of some ions in the observed AMD over a finite narrow ionization parameter space; e.g. at $\log \sim 1 - 2$ for IRAS 13349+2438 and NGC 3783 (e.g. Holczer et al. 2007) while $\log \xi \sim 2 - 2.8$ for Mrk 509 (e.g. Detmers et al. 2011). Since clouds are thought to be the products of a

thermal instability occurring in X-ray photoionized plasmas under constant pressure, the absence of transitions at specific ξ -values is often attributed to this instability. While these considerations have not been incorporated in our calculations, we would like to mention that our winds operate under conditions of constant density (locally), a situation not conducive to the aforementioned instability (e.g. Róžańska et al. 2006).

Figure 7 shows a calculated cooling curve for the bestfit photoionized wind of $p = 1.15$ under constant density thermal equilibrium; no thermal instability is apparent, typically indicated by a double-valued **S-shaped** region in the $\xi - \Xi$ space where $\Xi \equiv \xi/T$. The positions of the ions considered in this work (see **Tables 2-3**) are marked by the circles on the cooling curve at the derived values of ξ and T . Generally, under the thermal instability conditions, the observed ions should be associated with clouds in pressure equilibrium with hot gas. However, these occur under rather narrow regions in ξ inconsistent with the broad range of ionization values inferred from the observed transitions.

6. Summary

The line profiles of **Figures 2-3** highlight the success of our theoretical approach to model MHD-driven absorbers: (1) The properties of individual lines (i.e. shape and EW) are not independent; they were all computed with the same (and also help define the) global parameters of a wind that spans $10^5 - 10^6$ Schwarzschild radii in space and hence their physical conditions are all mutually coupled. (2) The detailed profiles of the lines are not symmetric (as they would be if fit with Gaussians or Voigt functions); they are skewed blueward in wavelength, a feature due to the combined variation of ionic abundances with ξ (they decrease faster beyond their maximum value and more gradually prior to that; see the AMD in **Fig. 1**) and the corresponding variation of the wind velocity with ξ , as expected in a continuous disk wind. The observed skewed profiles do reflect this property indicating that the velocity structure of the wind model is a reasonable representation of the real one. (3) The Fe xxv feature, usually a strong one in AGNs (Tombesi et al. 2013), is weak in NGC 3783. Our wind model reproduces the weakness of this line feature, in agreement with the observation.

In conclusion, the successful modeling of the absorbers of the AGN NGC 3783, along with those of the Galactic binary GRO J1655-40 (Fukumura et al. 2017), with the same global model, argues strongly for an underlying magnetized outflow of an invariant character, not unlike that of our MHD model. It is found, very similarly to the analysis for GRO J1655-40, that the wind is magnetically launched and accelerated with a global density structure of $n(r) = 6.9 \times 10^{11}(r/r_o)^{-1.15} \text{ cm}^{-3}$ with the viewing angle of 44° .

We note also that the possibility of MHD-driving disk-winds is independently discussed

in the context of the Fe K UFOs in the well-studied Seyfert 1 AGN, NGC 4151, by Kraemer et al. (2017), for example. Attributed to their typically high ionization parameter (e.g. $\log \xi \gtrsim 4.0$) and near-Compton thick column (e.g. $N_H \sim 10^{23-24} \text{ cm}^{-2}$), magnetic-origin seems to be a natural process especially for the UFOs as their study suggests. If a global magnetic field anchored to the underlying accretion disk is a generic component in AGNs/XRBs, then it is quite conceivable that the same magnetic field can play a significant role in launching the WAs discussed in this work for NGC 3783.

More detailed spectroscopic analyses of this kind will be made possible with the launch of *XARM* in the coming years and later on by ESA’s mission, *Athena*, through the micro-calorimeter observations. These missions will be able to better constrain the otherwise very enigmatic absorption properties with an unprecedented statistical significance perhaps leading to answering the ultimate question (partially if not fully) of launching mechanisms and the relations of the UV/X-ray absorbers seen in diverse AGNs.

We thank the anonymous referee for his/her constructive comments and questions. K.F. is grateful to Steve Kraemer, Travis Fischer and Patrick Hall for their insightful discussion on magnetically-launched X-ray winds in AGNs. F.T. acknowledges support by the Programma per Giovani Ricercatori - anno 2014 “Rita Levi Montalcini”. The research at the Technion is supported by the I-CORE program of the Planning and Budgeting Committee (grant number 1937/12). EB is grateful for the warm hospitality, support, and visiting professorship at the University of Maryland, College Park, and for funding from the European Union’s Horizon 2020 research and innovation programme under the Marie Skłodowska-Curie grant agreement no. 655324. This work is supported in part by NASA/ADAP (NNH15ZDA001N-ADAP) and *Chandra* AO17 archival proposal grants.

REFERENCES

- Adhikari, T. P., Rózańska, A., Sobolewska, M. & Czerny, B. 2015, The Extremes of Black Hole Accretion, Proceedings of the conference held 8-10 June, in Madrid, Spain, 815, 83
- Alloin, D. et al. *A&A*, 293, 293
- Begelman, M. C., McKee, C. F., & Shields, G. A. 1983, *ApJ*, 271, 70
- Behar, E. et al. 2003, *ApJ*, 598, 232
- Behar, E., 2009, *ApJ*, 703, 1346 (B09)
- Blandford, R. D. & Payne, D. G. 1982, *MNRAS*, 199, 883 (BP82)
- Blustin, A. J., Page, M. J., Fuerst, S. V., Branduardi-Raymont, G. & Ashton, C. E. 2005, *A&A*, 431, 111
- Casse, F. & Ferreira, J. 2000a, *A&A*, 353, 1115
- Casse, F. & Ferreira, J. 2000b, *A&A*, 361, 1178
- Chakravorty, S., Petrucci, P.-O., Ferreira, J., Henri, G., Belmont, R., Clavel, M., Corbel, S., Rodriguez, J., Coriat, M., Drappeau, S. & Malzac, J. 2016, *A&A*, 589, 119
- Chartas, G., Saez, C., Brandt, W. N., Giustini, M. & Garmire, G. P. 2009a, *ApJ*, 706, 644
- Chartas, G., Kochanek, C. S., Dai, X., Pointdexter, S. & Garmire, G. P. 2009b, *ApJ*, 693, 174
- Collinge, M. J. et al. 2001, *ApJ*, 557, 2
- Contopoulos, J. & Lovelace, R. V. E. 1994, *ApJ*, 429, 139 (CL94)
- Contopoulos, I., Kazanas, D. & Fukumura, K. 2017, *MNRAS*, 472, 20
- Couto, J. D., Kraemer, S. B., Turner, T. J. & Crenshaw, D. M. 2016, *ApJ*, 833, 191
- Crenshaw, D. M. et al. 1999, *ApJ*, 516, 750
- Crenshaw, D. M., Kraemer, S.B. & George, I. M. 2003 *Annu. Rev. Astron. & Astrophys.* 2003, 41, 117
- Crenshaw, D. M. & Kraemer, S. B. 2012, *ApJ*, 753, 75
- Detmers, R. G. et al. 2011, *A&A*, 534, 38

- Ferland, G. J., Porter, R. L., van Hoof, P. A. M., Williams, R. J. R., Abel, N. P., Lykins, M. L., Shaw, G., Henney, W. J. & Stancil, P. C. 2013, *Revista Mexicana de Astronomía y Astrofísica*, 49, 137
- Ferreira, J. 1997, *A&A*, 319, 340
- Fiore, F., Elvis, M., Mathur, S., Wilkes, B. J., & McDowell, J. C. 1993, *ApJ*, 415, 129
- Fukumura, K., Kazanas, D., Contopoulos, I. & Behar, E. 2010a, *ApJ*, 715, 636 (F10a)
- Fukumura, K., Kazanas, D., Contopoulos, I. & Behar, E. 2010b, *ApJ*, 723, L228 (F10b)
- Fukumura, K., Tombesi, F., Kazanas, D., Shrader, C., Behar, E. & Contopoulos, I. 2014, *ApJ*, 780, 120
- Fukumura, K., Tombesi, F., Kazanas, D., Shrader, C., Behar, E. & Contopoulos, I. 2015, *ApJ*, 805, 17
- Fukumura, K., Kazanas, D., Shrader, C., D., Behar, E., Tombesi, F. & Contopoulos, I. 2017, *Nature Astronomy*, 1, 0062
- Gabel, J. R. et al. 2003, *ApJ*, 583, 178
- Gabel, J. R. et al. 2005, *ApJ*, 631, 741
- George, I. M., Turner, T. J., Netzer, H., Nandra, K., Mushotzky, R. F., & Yaqoob, T. 1998, *ApJS*, 114, 73
- Gofford, J., Reeves, J. N., McLaughlin, D. E., Braitto, V., Turner, T. J., Tombesi, F. & Cappi, M. 2015, *MNRAS*, 451, 4169
- Gonçalves, A. C., Collin, S., Dumont, A.-M., Mouchet, M., Rózańska, A., Chevallier, L. & Goosmann, R. W. 2006, *A&A*, 451, 23
- Goosmann, R. W., Holczer, T., Mouchet, M., Dumont, A.-M., Behar, E., Godet, O., Gonçalves, A. C. & Kaspi, S. 2016, *A&A*, 589, 76
- Gupta, A., Mathur, S. & Krongold, Y. 2015, *ApJ*, 798, 4
- Halpern, J. P. 1984, *ApJ*, 287, 90
- Holczer, T., Behar, E. & Kaspi, S. 2007, *ApJ*, 663, 799
- Kaastra, J. S. 2014, *Science*, 345, 64
- Kallman, T. & Bautista, M. 2001, *ApJS*, 133, 221

- Kallman, T. R., Bautista, M. A., Goriely, S., Mendoza, C., Miller, J. M., Palmeri, P., Quinet, P. & Raymond, J. 2009, *ApJ*, 701, 865
- Kaspi, S., Brandt, W. N., Netzer, H., Sambruna, R., Chartas, G., Garmire, G. P. & Nousek, J. A. 2000, *ApJ*, 535, 17
- Kaspi, S., Brandt, W. N., Netzer, H., George, I. M., Chartas, G., Behar, E., Sambruna, R. M., Garmire, G. P. & Nousek, J. A. 2001, *ApJ*, 554, 261 (K01)
- Kaspi, S. et al. 2002, *ApJ*, 574, 643 (K02)
- Kazanas, D., Fukumura, K., Contopoulos, I., Behar, E. & Shrader, C. R. 2012, *Astronomical Review*, 7, 92
- Kazanas, D. 2015, *ASSL*, 414, 207
- Köngl, A. & Kartje, J. F. 1994, *ApJ*, 434, 446
- Kraemer, S. B., Crenshaw, D. M. & Gabel, J. R. 2001, *ApJ*, 557, 30
- Kraemer, S. B., Crenshaw, D. M., George, I. M., Netzer, H., Turner, T. J. & Gabel, J. R. 2002, *ApJ*, 577, 98
- Kraemer, S. B. & Crenshaw, D. M. 2012, *ApJ*, 753, 75
- Kraemer, S. B., Tombesi, F. & Bottorff, M. C. 2017, accepted to *ApJ* (arXiv:1711.07965)
- Krolik, J. H., McKee, C. F. & Tarter, C. B. 1981, *ApJ*, 249, 422
- Krongold, Y., Nicastro, F., Brickhouse, N. S., Elvis, M., Liedahl, D. A. & Mathur, S. 2003, *ApJ*, 597, 832
- Laha, S., Guainazzi, M., Dewangan, G. C., Chakravorty, S. & Kembhavi, A. K. 2014, *MNRAS*, 441, 2613
- Luketic, S., Proga, D., Kallman, T. R., Raymond, J. C. & Miller, J. M. 2010, *ApJ*, 719, 515
- Mathur, S., Wilkes, B., Elvis, M. & Fiore, F. 1994, *ApJ*, 434, 493
- Mathur, S., Elvis, M. & Wilkes, B. 1995, *ApJ*, 452, 230
- McKernan, B., Yaqoob, T. & Reynolds, C. S. 2007, *MNRAS*, 379, 1359
- Mehdipour, M. et al. 2017, accepted to *A&A*(arXiv:1707.04671)
- Miller, J. M. et al. 2006, *Nature*, 441, 953

- Miller, J. M. et al. 2008, *ApJ*, 680, 1359
- Miller, J. M., Fabian, A. C., Kaastra, J., Kallman, T., King, A. L., Proga, D., Raymond, J. & Reynolds, C. S. 2015, *ApJ*, 814, 87
- Murray, N., Chiang, J., Grossman, S. A. & Voit, G. M. 1995, *ApJ*, 451, 498
- Nandra, K., Pounds, K. A. 1992, *Nature*, 359, 215
- Nandra, K. et al. 1993, *MNRAS*, 260, 504
- Netzer, H. et al. 2003, *ApJ*, 599, 933
- Peterson, B. M., Ferrarese, L., Gilbert, K. M., Kaspi, S., Malkan, M. A., Maoz, D., Merritt, D., Netzer, H., Onken, C. A., Pogge, R. W., Vestergaard, M. & Wandel, A. 2004, *ApJ*, 613, 682
- Proga, D., Stone, J. M., & Kallman, T. R. 2000, *ApJ*, 543, 686
- Reeves, J. N., Nandra, K., George, I. M., Pounds, K. A., Turner, T. J. & Yaqoob, T. 2004, *ApJ*, 602, 648
- Reeves, J. N., O’Brien, P. T., Braitto, V., Behar, E., Miller, L., Turner, T. J., Fabian, A. C., Kaspi, S., Mushotzky, R. & Ward, M. 2009, *ApJ*, 701, 493
- Reynolds, C. S., Fabian, A. C., Nandra, K., Inoue, H., Kunieda, H., & Iwasawa, K. 1995, *MNRAS*, 277, 901
- Reynolds, C. S., Ward, M. J., Fabian, A. C., & Celotti, A. 1997, *MNRAS*, 291, 403
- Rózańska, A., Goosmann, R., Dumont, A.-M. & Czerny, B. 2006, *A&A*, 452, 1
- Scott, A. E., Brandt, W. N., Behar, E., Crenshaw, D. M., Gabel, J. R., Gibson, R. R., Kaspi, S., Kraemer, S. B. & Turner, T. J. 2014, *ApJ*, 797, 105
- Steenbrugge, K. C., Kaastra, J. S., Crenshaw, D. M., Kraemer, S. B., Arav, N., George, I. M., Liedahl, D. A., van der Meer, R. L. J., Paerels, F. B. S., Turner, T. J. & Yaqoob, T. 2005, *A&A*, 434, 569
- Stern, J., Behar, E., Laor, A., Baskin, A. & Holczer, T. 2014, *MNRAS*, 445, 3011
- Tombesi, F., Cappi, M., Reeves, J. N., Palumbo, G. G. C., Yaqoob, T., Braitto, V. & Dadina, M. 2010, *A&A*, 521, 57
- Tombesi, F., Cappi, M., Reeves, J. N., Nemmen, R. S., Braitto, V., Gaspari, M. & Reynolds, C. S. 2013, *MNRAS*, 430, 1102

Tombesi, F., Meléndez, M., Veilleux, S., Reeves, J. N., González-Alfonso, E. & Reynolds, C. S. 2015, *Nature*, 519, 436

Turner, T. J., Nandra, K., George, I. M., Fabian, A. C. & Pounds, K. A. 1993, *ApJ*, 419, 127

Turner, T. J., Kraemer, S. B., George, I. M., Reeves, J. N. & Bottorff, M. C. 2005, *ApJ*, 618, 155